Optical method for measuring the volume fraction of granular media: Application to faced-centered cubic lattices of monodisperse spheres

L. Sarno,[1,2,*] L. Carleo,[1] M. N. Papa [ORCID],[1] and A. Armanini[3]

[1]*Department of Civil Engineering, University of Salerno, 84084 Fisciano, Italy*
[2]*Institute of Fluid Dynamics (FDY), Technische Universität Darmstadt, 64287 Darmstadt, Germany*
[3]*Department of Civil, Environmental and Mechanical Engineering, CUDAM, University of Trento, 38123 Trento, Italy*

In order to understand the dynamics of granular flows, one must have knowledge about the solid volume fraction. However, its reliable experimental estimation is still a challenging task. Here, we present the application of a stochastic-optical method (SOM) [L. Sarno *et al.*, Granul. Matter **18**, 80 (2016)] to an array of spheres arranged according to faced-centered cubic lattices, where spheres' locations are known *a priori*. The purpose of this study is to test the robustness of the image binarization algorithm, introduced in the SOM for the indirect estimation of the near-wall volume fraction through an optically measurable quantity, defined as *two-dimensional* volume fraction. A comprehensive range of volume fractions and illumination conditions are numerically and experimentally investigated. The proposed binarization algorithm is found to yield reasonably accurate estimations of the two-dimensional volume fraction with a root-mean-square error smaller than 0.03 for all investigated illumination conditions. A slightly worse performance is observed for samples with relatively low volume fractions (<0.3), where the binarization algorithm occasionally cannot identify the surface elements in the second and third layers of the regular lattice.

I. INTRODUCTION

Granular media are ubiquitous in natural phenomena (e.g., debris flows and avalanches) and in industrial applications (e.g., conveyance of pellets, silo discharge, etc.). Clearly, the dynamics of such systems is subject to the laws of classical mechanics, but it is still far from being completely understood due to complex momentum exchange mechanisms [1–5]. In recent years several efforts have been made to study the dynamics of granular media from theoretical and experimental viewpoints [6–13]. In addition to the increasing numerical studies with discrete element models (DEM) [14–18], the experimental investigation, on quantities such as the velocity and the solid volume fraction, still represents an irreplaceable tool for understanding the granular dynamics and for validating mathematical models.

With reference to a representative volume, the solid volume fraction is the ratio between the volume occupied by grains and the total volume of the mixture. At the grain scale, the local volume fraction can be defined as the ratio between the volume occupied by a single grain and the volume of the polyhedron, resulting from a Voronoï 3D tessellation on the grains' centers [19,20]. In standard laboratories cost-effective techniques for investigating granular flows are typically of the optical type. With the notable exception of refractive index-matching methods requiring transparent granular mixtures [21–23], the measurement of the velocity and volume fraction by optical methods is only possible at the boundaries of

the flow domain. If the flow dynamics at the boundaries is not representative of the whole flow field, this restraint may become relevant. To this regard, slow dense flows in narrow geometries are found to be approximately uniform along the transverse direction [24], while in the granular flows governed by gravity, significant concentration gradients were observed near the free surface [12,25]. On the other hand, it is worth mentioning that rapid granular flows in wide channels may develop heterogeneous patterns due to the onset of transverse flow instabilities, e.g., the self-supported regime with a dense core surrounded by dilute regions at the boundaries, reported by Brodu *et al.* [26].

Reasonably accurate estimations of the velocity field at the sidewall and at the free surface of granular currents are achievable today thanks to mature measurement techniques, such as the particle tracking velocimetry, PTV [12,19,27] and the particle image velocimetry, PIV [28–33]. Conversely, the measurement of the solid volume fraction is much more difficult. In the last decades only few optical methods have been introduced for approximate estimations of the volume fraction [19,20,34–38], and, to date, there is still no consensus on the most appropriate approach. Sarno *et al.* [39] proposed a stochastic-optical method (SOM) for estimating the volume fraction in an indirect way. Namely, they found that the volume fraction, c_{3D}, related to a finite reference volume delimited by a transparent planar wall, can be estimated by means of a measurable correlated quantity, called the two-dimensional (2D) volume fraction c_{2D}. This quantity is evaluable from photographs taken under controlled illumination conditions. Extensive numerical simulations, carried out by using the Monte Carlo (MC) method, allowed them to identify a clear

---
*Corresponding author: sarno@fdy.tu-darmstadt.de

stochastic relationship between c_{2D} and c_{3D}. To provide an averaged estimation of c_{3D}, the SOM requires a sufficiently large number of c_{2D} measurements. For the utilization of the SOM in real laboratory investigations, an automatic-vision binarization algorithm was proposed in Ref. [39] so as to be able to obtain c_{2D} from gray-scale digital images. Similar to other optical techniques, the laboratory employment of the SOM method involves facing some uncertainties. First, the theoretical transfer function between c_{2D} and c_{3D} has been numerically obtained under ideal assumptions (e.g., perfect spherical grains; perfectly parallel light beams etc.), which are not rigorously fulfilled in a laboratory environment. Another possible source of error is the binarization algorithm itself.

The SOM method was successfully validated by [39] on randomly dispersed liquid-granular mixtures, composed of plastic (POM) beads immersed in a water-sucrose solution, and also on random dry granular packings. More recently, Sarno *et al.* [40] further investigated the performance of the SOM on randomly dispersed POM mixtures by employing rectangular interrogation windows with different aspect ratios. This latter study confirmed the good capabilities of the SOM in estimating the averaged c_{3D}. Yet, in comparison to analogous numerical simulations, slightly larger scatter of the estimations were found, probably due to errors introduced by the image binarization strategy.

Motivated by these observations, in the present work we specifically focus on the binarization algorithm, implemented in the SOM. An experimental study on regular lattices of monodisperse spheres immersed in air is here presented. Such lattices were built according to the faced-centered cubic (FCC) pattern and are composed of perfect spheres, held together with thin nylon wires. Thanks to the regular FCC pattern, the relationship between c_{2D} and c_{3D} is not stochastic but totally deterministic. Consequently, this arrangement allowed us to assess the performance of the binarization algorithm.

The paper is composed of the following parts. The principles of the SOM method are briefly recalled in Sec. II. Section III describes the application to regular FCC lattices. In particular, the deterministic transfer functions, found for FCC lattices, are reported together with a description of the experimental setup. In Sec. IV the results are presented and discussed. The conclusions are summarized in Sec. V.

II. THE STOCHASTIC-OPTICAL METHOD (SOM)

Here the rationale of the SOM method is briefly recalled. For further details we refer the reader to Refs. [39–41]. Considering a transparent wall, Δ, delimiting the granular domain, the SOM method requires controlled illumination conditions, so as to be able to estimate the near-wall volume fraction, c_{3D}, through a correlated quantity, called the two-dimensional volume fraction, c_{2D}. The measurement of this quantity requires the following experimental setup (Fig. 1):

(1) A digital camera located in front of the transparent wall and sufficiently far from it, so that the perspective changes of the size of grains, located at different distances from the wall, are negligible in the imaging plane;

(2) A no-flicker planar lamp that illuminates the wall from a constant direction with angle of incidence, ζ.
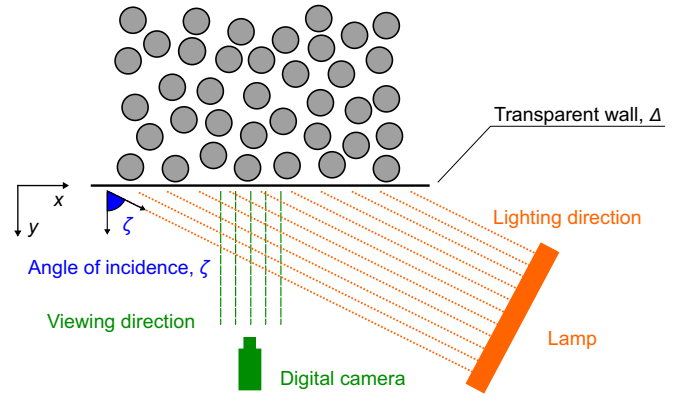
FIG. 1. Sketch of the experimental setup for the SOM method. The viewing direction is normal to Δ, while ζ is the angle between viewing and lighting directions.

With reference to Fig. 1, c_{2D} is defined as the ratio between the projected area on the interrogation window (IW) of all surface elements, concurrently visible and directly illuminated, and the total IW area. Since the SOM works similarly to a triangulation method [42], it is crucial that the angle, ζ, between viewing and lighting directions is non-null. A numerical investigation, employing the MC method for generating random distributions of spheres, allowed Sarno *et al.* [39] to identify a stochastic relationship between c_{2D} and c_{3D}

$$c_{3D} = a(\zeta)\exp(b(\zeta)\,c_{2D}), \qquad (1)$$

where a is found to be proportional to $1/\cos(\zeta)$ and b weakly depends on ζ. In that investigation c_{3D} could be exactly calculated with reference to a finite cubic volume delimited by Δ, and c_{2D} was determined by purely geometric arguments on an IW, corresponding to the front face of the same cubic volume. Thanks to the randomness of the spheres' locations, the illumination condition could be fully characterized by the angle of incidence ζ.

The transfer function (1) is of stochastic type: thus, for each value of c_{3D}, c_{2D} exhibits some scatter around its average (cf. Fig. 4 in Ref. [39]). This dispersion may be described by the standard deviation of c_{2D}, $\sigma_{c_{2D}}(c_{3D})$, or more synthetically by its average, $\overline{\sigma_{c_{2D}}}$, calculated over the entire interval of the investigated volume fractions. From the viewpoint of the measurement accuracy, a low sensitivity of c_{2D} on c_{3D}, $d(c_{3D})/d(c_{2D})$ [i.e., the derivative of Eq. (1) with respect to the input variable c_{2D}], and a low c_{2D} scatter are desirable properties of the function (1). In a previous work Sarno *et al.* [39] systematically studied the behavior of the transfer function over a wide range of ζ (between 5° and 70°). It emerged that an increase of ζ also causes an increase of the scatter of c_{2D} (particularly relevant for $\zeta > 60°$), while values of ζ smaller than 10° lead to the saturation of c_{2D} in the upper part of the transfer curve (cf. Table 1 and Fig. 4 in Ref. [39]). These trends at the extreme ends are clearly undesirable for the accuracy of the method and indicate that an intermediate range of ζ is preferable for applications.

To practically estimate c_{2D} by using a digital camera in real laboratory applications, it is crucial that the main light source, coming from a controlled direction, is much brighter than the environmental light, so as to avoid unwanted influences on

the images' exposure. Moreover, gray-scale digital pictures need to be suitably binarized. A local binarization algorithm, depending on the brightness values within a small neighborhood of each pixel, was proposed in Ref. [39]. This algorithm works locally with the aim of reducing undesired effects from slightly uneven light intensities in the region of interest (ROI). The binarized image, B, is defined as

$$B_{i,j} = \left(\frac{O'_{i,j} - O'_{\min,N(i,j)}}{O'_{\max,N(i,j)} - O'_{\min,N(i,j)}} > s \right), \quad (2)$$

where $O'_{i,j}$ is the brightness of the pixel (i, j) in the γ-decoded image $O' = O^{1/\gamma}$, $O'_{\min,N(i,j)}$ and $O'_{\max,N(i,j)}$ are the minimum and maximum brightnesses in a circular neighborhood N of (i, j) of diameter D_N. In Eq. (2) s is a parameter to be experimentally calibrated. A limitation of formula (2) consists in the low robustness against occasional spikes of $O'_{\max,N(i,j)}$, due to glare on the grains' surface. This problem is more relevant if the grains exhibit some direct reflectance or if the interstitial fluid is highly transparent. An improvement of Eq. (2) consists in the calculation of the local maximum brightness, not on O', but on a preprocessed image O'', obtained by a suitable moving average filter (MAF)

$$O'' = O'_{\text{avg}, [p_x, p_z]}. \quad (3)$$

To reduce border effects in the application of the MAF, the brightness values outside the boundaries of the ROI are computed by mirror-reflecting the brightness values across the boundary. Sarno *et al.* [39] reported that a squared average filter of size $p = p_x = p_z \approx 0.2d$ was sufficient to get reliable results on matte white POM plastic beads with very low direct reflectance. Investigating random granular dispersions by using rectangular IWs with different aspect ratios, in Ref. [40] it was observed that a larger MAF seems to be beneficial for improving the accuracy of the binarization strategy.

Once the binarized image B is obtained from Eqs. (2) and (3), the value of c_{2D} can be simply calculated as

$$c_{2D} = \frac{\sum_N B_{i,j}}{N}, \quad (4)$$

where N is the total number of pixels in the IW.

The experimental validation, carried out by Sarno *et al.* [39,40], showed a very good performance of the modified binarization algorithm [Eqs. (2),(3)] on randomly dispersed POM beads. Yet, it was observed that the experimental standard deviations, $\sigma_{c_{2D}}(c_{3D})$ are generally higher than the ones numerically obtained from MC simulations. These discrepancies are probably due to the fact that the binarization algorithm occasionally fails to identify some illuminated surface elements and, thus, add up random errors to the natural fluctuations of c_{2D}. On the other hand, these possible flaws of the binarization strategy could have been obscured by other error sources, intrinsic to the previous experimental arrangements, e.g., a nonperfectly homogenous optical response of the grains or their nonperfectly spherical shape. These observations motivated us to look in more detail at the performance of the binarization algorithm on regular lattices, where the spheres' locations are known *a priori*.
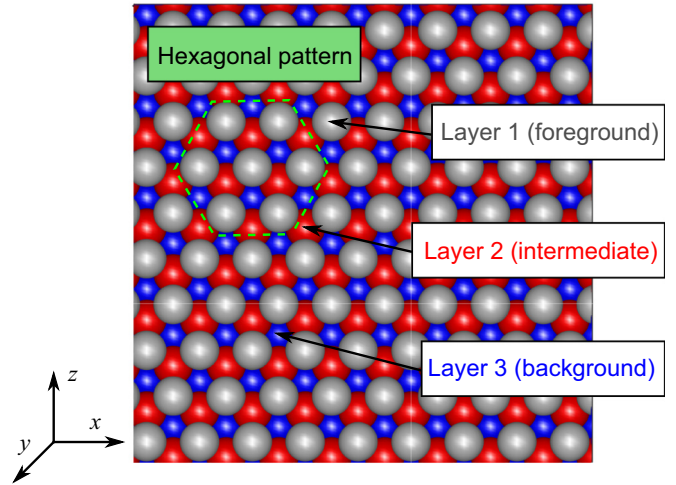
FIG. 2. Centered FCC disperse lattice of equal spheres (∇-type orientation) with $\lambda = 1.33$.

III. APPLICATION OF THE SOM TO REGULAR LATTICES

A. FCC lattices

Two regular lattices are suitable for closely packing equal spheres: the FCC and the hexagonal close packing (HCP). Considering a system of equal spheres, it has been conjectured [43] and proved more recently [44] that FCC and HCP lattices yield the maximum possible average volume fraction, $\pi/\sqrt{18} \approx 0.74$. If the same lattices are constructed with closely packed virtual spheres of diameter D and, subsequently, smaller spheres of diameter $d < D$ are positioned in such a way that their centers coincide with the centers of the large spheres, one obtains dispersed deterministic distributions, where the spheres are not in direct contact with each other. The resulting volume fraction is smaller than the maximum packing and can be evaluated by the following asymptotic formula, valid for an infinitely large reference volume

$$c_{\text{3D,asympt}}(D/d) = \frac{\pi}{\sqrt{18}} \left(\frac{d}{D} \right)^3 = \frac{\pi}{\sqrt{18}} \lambda^{-3}. \quad (5)$$

In Eq. (5) the diameter ratio, $\lambda = D/d$, is the so-called *linear concentration* [45] and is isotropic in space. Some deviation from Eq. (5) occurs if a reference volume of finite size is considered. An example of a disperse FCC structure is sketched in Fig. 2, where the spheres' diameter is $d = 0.75D$ ($c_{\text{3D,asympt}} \approx 0.31$). Considering the frame of reference of Fig. 2, the FCC lattice is composed of different layers parallel to the xz plane. In all layers the spheres are arranged in a honeycomb-like hexagonal tessellation, formed of six equilateral triangles of side D. The distance between two layers is $\sqrt{6}D/3$ owing to the tetrahedral arrangement of four adjacent spheres. The structure of the FCC lattice is such that the xz patterns repeat in space with periodicity 3. Consequently, for all λ, the first three layers are visible by a transparent wall, parallel to the xz plane. Conversely, in HCP lattices the layers' periodicity is

TABLE I. List of the investigated illumination conditions.

ID	Azimuth, α [deg]	Tilt, τ [deg]	ζ [deg]
POS-1	25.0	0.0	25.0
POS-2	30.0	5.0	30.4
POS-3	30.0	15.0	33.2
POS-4	30.0	25.0	38.3

TABLE II. List of the investigated FCC virtual samples.

ID	$\lambda = D/d$	$c_{3D,asympt}$	Near-wall c_{3D}
S-virt-1	2.100	0.080	0.073
S-virt-2	1.963	0.098	0.100
S-virt-3	1.913	0.106	0.112
S-virt-4	1.863	0.115	0.122
S-virt-5	1.750	0.138	0.140
S-virt-6	1.606	0.179	0.184
S-virt-7	1.500	0.219	0.222
S-virt-8	1.431	0.253	0.251
S-virt-9	1.375	0.285	0.282
S-virt-10	1.306	0.332	0.336
S-virt-11	1.250	0.379	0.374
S-virt-12	1.219	0.409	0.407
S-virt-13	1.188	0.442	0.435
S-virt-14	1.163	0.471	0.470
S-virt-15	1.138	0.503	0.502
S-virt-16	1.106	0.547	0.542
S-virt-17	1.075	0.596	0.590
S-virt-18	1.038	0.663	0.646
S-virt-19	1.019	0.700	0.687
S-virt-20	1.000	0.740	0.727

2. Considering that FCC lattices allow deeper visibility inside the domain than HCP ones, the FCC structure is chosen for the present investigation.

B. Transfer function c_{2D}-c_{3D} for regular FCC lattices

Before using the SOM on regular lattices, it is worth underlining some important distinctions from the case of randomly distributed spheres. Owing to the regularity of the lattice, the relationship between c_{2D} and c_{3D} is not stochastic but deterministic. Thus, Eq. (1) ceases to be valid. Moreover, the new relationship (c_{2D}, c_{3D}) crucially depends on the geometrical structure of the lattice and also on the orientation of the lattice tessellation in the xz plane with respect to light direction. In fact, the locations of the foreground spheres influence the optical penetration and, consequently, c_{2D}. Hence, different from random distributions, the illumination setup cannot be characterized by the sole angle of incidence, ζ, but requires the specification of the light direction. In Fig. 2 the subgroups, composed of three spheres of layer 1 (gray colored) and one sphere of layer 2 (red colored) in the middle, form triangles with upper side parallel to the x axis. This orientation, referred to as ∇ type, will be employed hereafter.

To identify the deterministic transfer functions, a numerical investigation was performed on 20 virtual FCC samples corresponding to c_{3D} values from ≈ 0.05 to ≈ 0.73. Four illumination settings, with the angle of incidence of the light in the intermediate range $20° < \zeta < 40°$, were investigated (Table I). In order to fully define the direction of the light rays with respect to the ∇-type lattice orientation, the angle of incidence, ζ, is decomposed into two angles: *azimuth*, α, and *tilt*, τ. The azimuth, α, is defined as the angle between the normal to the vertical transparent wall and the projection on the horizontal xy plane of the light direction, while τ is the vertical inclination of the light rays with respect to the horizontal. The positive clockwise convention is considered, i.e., $\alpha > 0$ if the light comes from the first quadrant of the xy plane and $\tau > 0$ if the light rays are oriented from top downwards with respect to the FCC sample. It can be easily verified that $\zeta = \arccos(\cos\alpha \cos\tau)$.

For each virtual sample, the FCC lattice was generated in a cube of side $15d$, from which a smaller cube of side $7.5d$ was cropped. This smaller cube, delimited by the planar surface Δ (corresponding to the transparent wall) parallel to xz and tangent to the first layer of spheres, was considered for the estimation of c_{3D}. The complete list of the virtual samples is reported in Table II, together with $\lambda = d/D$, $c_{3D,asympt}$ calculated by Eq. (5), and the near-wall volume fraction c_{3D}, estimated by considering the effective volume of the cube of side $7.5d$. For each virtual sample, the calculations of c_{2D} were carried out from different squared IWs of size $5d \times 5d$,

obtained by shifting a $5d \times 5d$ square by steps of $0.125d$ in both x and z directions.

(a)

(b)

FIG. 3. (a) Relationships (c_{2D}, c_{3D}) for FCC deterministic lattices ($5d \times 5d$ IWs). The averages of c_{2D} are reported together with their minimum and maximum values, obtained by shifting the IW in a range $\pm 1.25d$ along x and z directions. (b) Standard deviations $\sigma_{c_{2D}}(c_{3D})$. Inset: averaged standard deviations, $\overline{\sigma_{c_{2D}}}$.
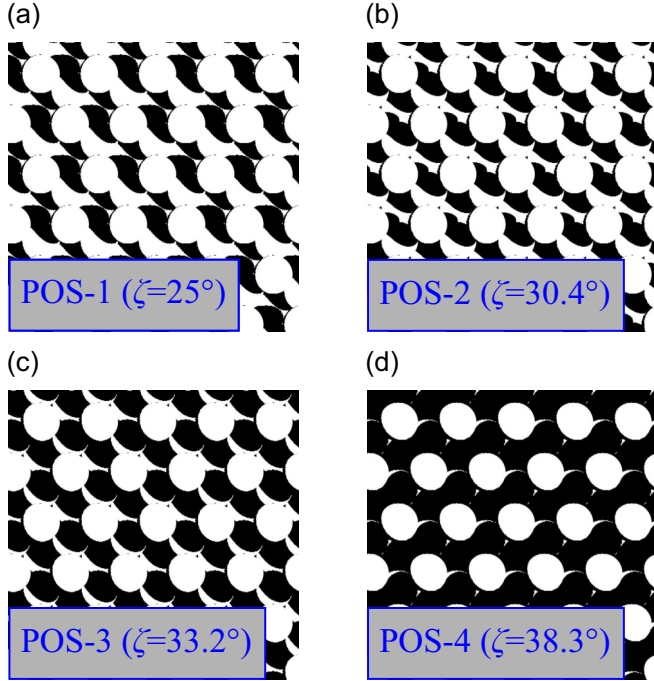
FIG. 4. Binarized images of S-virt-7 ($c_{3D} = 0.222$) under different illumination conditions. White pixels correspond to visible and illuminated surface elements, concurring to c_{2D} calculation. (a) POS-1; (b) POS-2; (c) POS-3; (d) POS-4.

The transfer functions for the four illumination conditions (cf. Table I) are reported in Fig. 3. For each c_{3D}, the average values of c_{2D} are shown together with the range of variation of c_{2D}, i.e., the range between minimum and maximum values [Fig. 3(a)]. Additionally, $\sigma_{c_{2D}}(c_{3D})$ are reported in Fig. 3(b), while Fig. 3(c) shows the averages $\overline{\sigma_{c_{2D}}}$ calculated over the entire range of c_{3D}. It can be noted that the deterministic transfer functions significantly differ from the exponential ones of type (1), valid for random spheres' distributions [Fig. 3(a)]. From Fig. 3(b), it emerges that $\sigma_{c_{2D}}$ generally decreases with increasing c_{3D}. Although some oscillations occur due to the regular structure of the lattice, this trend is analogous to that observed in random dispersions of spheres [40]. For illustration, Fig. 4 reports the numerically binarized images of the virtual sample S-virt-7.

C. Laboratory investigation on FCC samples

The details of the laboratory investigation on FCC lattices are here reported. The experimental samples are built up of plastic spheres with diameter $d = 8$ mm. Different from the matte white POM beads, employed in Refs. [39–41], the spheres of this campaign are characterized by a glossy finish with some specular direct reflectance. Thus, the optical properties of the employed granular material represented a challenging test bench for the binarization algorithm. A small cylindrical hole, passing from one side to the other of each sphere, allowed that the spheres were held together by thin barely visible nylon wires of thickness of 0.5 mm, so as to form dispersed FCC lattices with various volume fractions ($\lambda \geqslant 1$). The relative locations of the spheres were precisely

TABLE III. List of the experimental samples, made up of white spheres arranged in dispersed FCC lattices.

ID	Virtual sample	D [mm]	$\lambda = D/d$	$c_{3D,asympt}$	Near-wall c_{3D}
S-1	S-virt-5	14	1.750	0.138	0.140
S-2	S-virt-7	12	1.500	0.219	0.222
S-3	S-virt-9	11	1.375	0.285	0.282
S-4	S-virt-11	10	1.250	0.379	0.374
S-5	S-virt-13	9.5	1.188	0.442	0.435
S-6	S-virt-15	9.1	1.138	0.503	0.502
S-7	S-virt-17	8.6	1.075	0.596	0.590
S-8	S-virt-20	8.0	1.000	0.740	0.727

determined by using rigid templates. In the samples' construction we progressively increased the distances, D, between the spheres' centers, $D = \lambda d$. Eight laboratory samples with $0.14 < c_{3D} < 0.73$ were prepared (Table III). These experimental samples correspond to a subset of the virtual samples of Table II. For convenience, the corresponding codes of the virtual samples are also recalled in Table III.

Before each investigation, the sample was placed on a horizontal plane behind a vertical 10-mm-thick Plexiglas wall, so that the layers of the lattice were parallel to the xz plane with ∇-type orientation (cf. Fig. 2). The first layer of spheres was set tangential to the anterior transparent wall. The instrumentation is composed of a high-speed camera (Photron Fastcam-1024PCI model 100 K, with resolution 1024×1024 pixels and 8-bit depth) and a no-flicker planar LED lamp (model Photo-Sonics MultiLED-LT) with a luminous output of ≈ 7700 lumens, allowing a camera shutter time of 15 μs. In order to correctly apply the binarization algorithm, we had to ensure that all the spheres in the pictures were in focus [39]. Specifically, we checked that the camera's depth of field encompassed the first three layers of the lattice even in the most disperse case, i.e., the sample S-1 with $D = 1.75d = 14$ mm. Hence, by adjusting the lens aperture, the depth of field
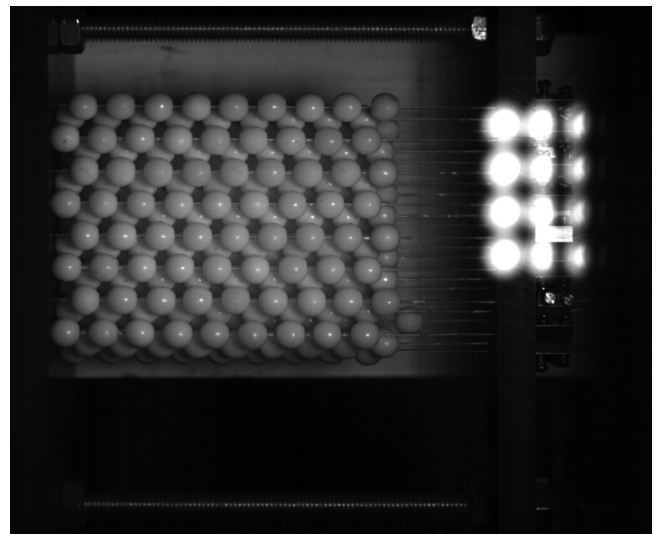
FIG. 5. Picture of the sample S-4 ($c_{3D} = 0.374$) taken under the illumination condition POS-1.

TABLE IV. Best-fitting binarizations for the lamp position POS-1 ($\alpha = 25°$, $\tau = 0°$, $\zeta = 25.0°$).

D_N	p	s	RMSE$_{c2D}$	$\overline{\sigma_{c2D}}$
	0.2d	0.432	0.033	0.006
	0.5d	0.485	0.028	0.006
1.0d	1.0d	0.636	0.024	0.006
	1.5d	**0.678**	**0.020**	**0.005**
	2.0d	0.693	0.022	0.005
	0.2d	0.418	0.038	0.008
	0.5d	0.469	0.034	0.007
1.5d	1.0d	0.624	0.025	0.009
	1.5d	**0.676**	**0.018**	**0.006**
	2.0d	0.696	0.021	0.006
	0.2d	0.414	0.042	0.009
	0.5d	0.467	0.037	0.008
2.0d	1.0d	0.621	0.026	0.010
	1.5d	**0.670**	**0.018**	**0.008**
	2.0d	0.694	0.021	0.007

TABLE VI. Best-fitting binarizations for the lamp position POS-3 ($\alpha = 30°$, $\tau = 15°$, $\zeta = 33.2°$).

D_N	p	s	RMSE$_{c2D}$	$\overline{\sigma_{c2D}}$
	0.2d	0.328	0.042	0.010
	0.5d	0.373	0.039	0.009
1.0d	1.0d	0.543	0.032	0.008
	1.5d	**0.625**	**0.020**	**0.007**
	2.0d	0.638	0.020	0.007
	0.2d	0.306	0.054	0.010
	0.5d	0.346	0.052	0.010
1.5d	1.0d	0.525	0.038	0.010
	1.5d	**0.617**	**0.017**	**0.009**
	2.0d	0.638	0.020	0.008
	0.2d	0.306	0.060	0.011
	0.5d	0.347	0.057	0.011
2.0d	1.0d	0.515	0.042	0.011
	1.5d	**0.610**	**0.016**	**0.010**
	2.0d	0.634	0.019	0.009

was set slightly larger than $d/2 + 2(\sqrt{6} \times 1.75d/3) \approx 27\,\mathrm{mm}$ and, then, was kept constant in the entire experimental campaign. Two tripods, equipped with adjustable geared heads (Manfrotto Junior 410), are used for precisely positioning the camera and the lamp. Preliminary tests on a matte gray card were carried out to estimate the camera's γ-encoding function [39]. The best-fitting value is found $\gamma \approx 1.0$ for the entire brightness range ($\approx 30 - 200$), observed in the photographs of the present study. An example picture of the sample S-4 is reported in Fig. 5.

The same four lamp positions, listed in Table I, were also employed in the experimental campaign. With reference to the chosen lamp positions, it should be noted that, in our specific experimental setup, angles of incidence smaller than 25° could not be used, due to interferences between the tripods of the camera and of the LED lamp. The LED lamp was carefully placed, so that its center had a distance

of 32 cm from the center of the ROI. Its position was verified by trigonometric methods with an accuracy of $\approx 1\,\mathrm{mm}$. Analogous to the numerical investigation, c_{2D} was evaluated on squared IWs of side $5d$. In order to get a sufficiently large number of c_{2D} estimations, each sample was photographed 50 times, by shifting it with respect to the camera ROI thanks to a system of gears. For each lamp position, each sample was shifted vertically and horizontally by $\approx 20\,\mathrm{mm} = 2.5d$ with displacement steps of $\approx 3\,\mathrm{mm}$, so that the total span, encompassed by the photographs, was $\approx 7.5d$, analogous to the numerical investigation of Sec. III B.

IV. RESULTS AND DISCUSSION

A. Best settings of the binarization algorithm

The modified binarization algorithm, composed of Eqs. (2) and (3), is employed with different settings. Specifically, we

TABLE V. Best-fitting binarizations for the lamp position POS-2 ($\alpha = 30°$, $\tau = 5°$, $\zeta = 30.4°$).

D_N	p	s	RMSE$_{c2D}$	$\overline{\sigma_{c2D}}$
	0.2d	0.392	0.037	0.007
	0.5d	0.440	0.034	0.007
1.0d	1.0d	0.600	0.032	0.007
	1.5d	**0.661**	**0.016**	**0.005**
	2.0d	0.675	0.020	0.005
	0.2d	0.372	0.047	0.008
	0.5d	0.420	0.044	0.007
1.5d	1.0d	0.585	0.035	0.009
	1.5d	**0.657**	**0.016**	**0.007**
	2.0d	0.676	0.020	0.006
	0.2d	0.370	0.051	0.009
	0.5d	0.417	0.048	0.008
2.0d	1.0d	0.579	0.037	0.011
	1.5d	**0.652**	**0.016**	**0.008**
	2.0d	0.675	0.021	0.007

TABLE VII. Best-fitting binarizations for the lamp position POS-4 ($\alpha = 30°$, $\tau = 25°$, $\zeta = 38.3°$).

D_N	p	s	RMSE$_{c2D}$	$\overline{\sigma_{c2D}}$
	0.2d	0.372	0.037	0.011
	0.5d	0.424	0.038	0.010
1.0d	**1.0d**	**0.616**	**0.030**	**0.009**
	1.5d	0.666	0.061	0.008
	2.0d	0.690	0.057	0.008
	0.2d	0.355	0.025	0.011
	0.5d	0.406	0.024	0.011
1.5d	**1.0d**	**0.599**	**0.024**	**0.010**
	1.5d	0.662	0.058	0.009
	2.0d	0.690	0.056	0.009
	0.2d	0.355	0.026	0.012
	0.5d	0.406	0.024	0.012
2.0d	**1.0d**	**0.593**	**0.024**	**0.011**
	1.5d	0.654	0.057	0.010
	2.0d	0.685	0.054	0.009
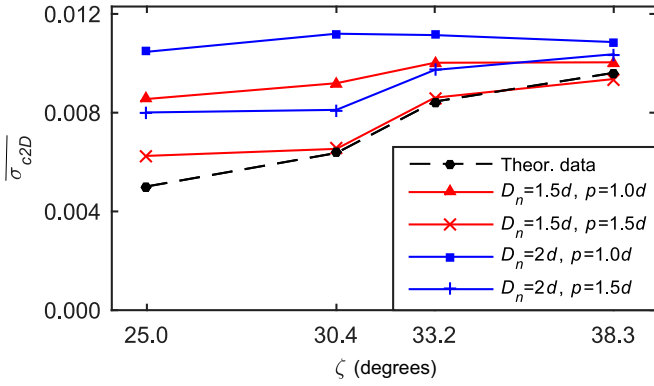
FIG. 6. Comparisons between experimental and theoretical values of $\overline{\sigma_{c_{2D}}}$ for various angles of incidence of light, ζ.

varied the span of the pixel neighborhood, D_N, and the size of the MAF, p. The following values of D_N are investigated: $1.0d$, $1.5d$, $2.0d$. Preliminary investigations revealed that a neighborhood smaller than $1d$ causes large inaccuracies in the binarization task. Additionally, five sizes of the MAF are investigated: $0.2d$, $0.5d$, $1.0d$, $1.5d$, $2.0d$. For each combination of D_N, p, and light direction, the best-fitting threshold s in Eq. (2) was found by minimizing the root-mean-square error (RMSE) between the averaged experimental estimations of

c_{2D}, $\overline{c_{2D,exp}}$, obtained from different photographs of the eight samples, and the corresponding averaged values, $\overline{c_{2D,num}}$, obtained numerically [cf. Fig. 3(a)]

$$\text{RMSE}_{c_{2D}} = \sqrt{\frac{\sum_{i=1}^{8} (\overline{c_{2D,exp}} - \overline{c_{2D,num}})^2}{8}}. \qquad (6)$$

As we are interested in evaluating the accuracy of the binarization algorithm, different from Ref. [39], here we used the RMSE on c_{2D} ($\text{RMSE}_{c_{2D}}$) as optimization criterion, instead of the RMSE on c_{3D}, which conversely is defined by replacing c_{2D} with c_{3D} in Eq. (6). Clearly, the advantage of using the RMSE on c_{2D} is that it allows to evaluate the isolated performance of the image binarization algorithm before the application of the transfer function. The best-fitting binarizations, corresponding to lamp positions POS-1, POS-2, POS-3, and POS-4, are reported in Tables IV – VII, respectively. For each investigated D_N the best setting for p is reported in bold.

It can be noted that, while the best-fitting value of s is less insensitive to the choice of D_N, it increases with p. Indeed, as follows from Eq. (2), s varies with the maximum brightness, which in turn depends on the size of the MAF. By comparing the same binarization settings for various light directions, slightly different values of s were observed, unlike the previous investigations on POM beads [39], where an almost constant s was found for a comparable range of ζ. This behavior is due to the fact that the spheres of the present
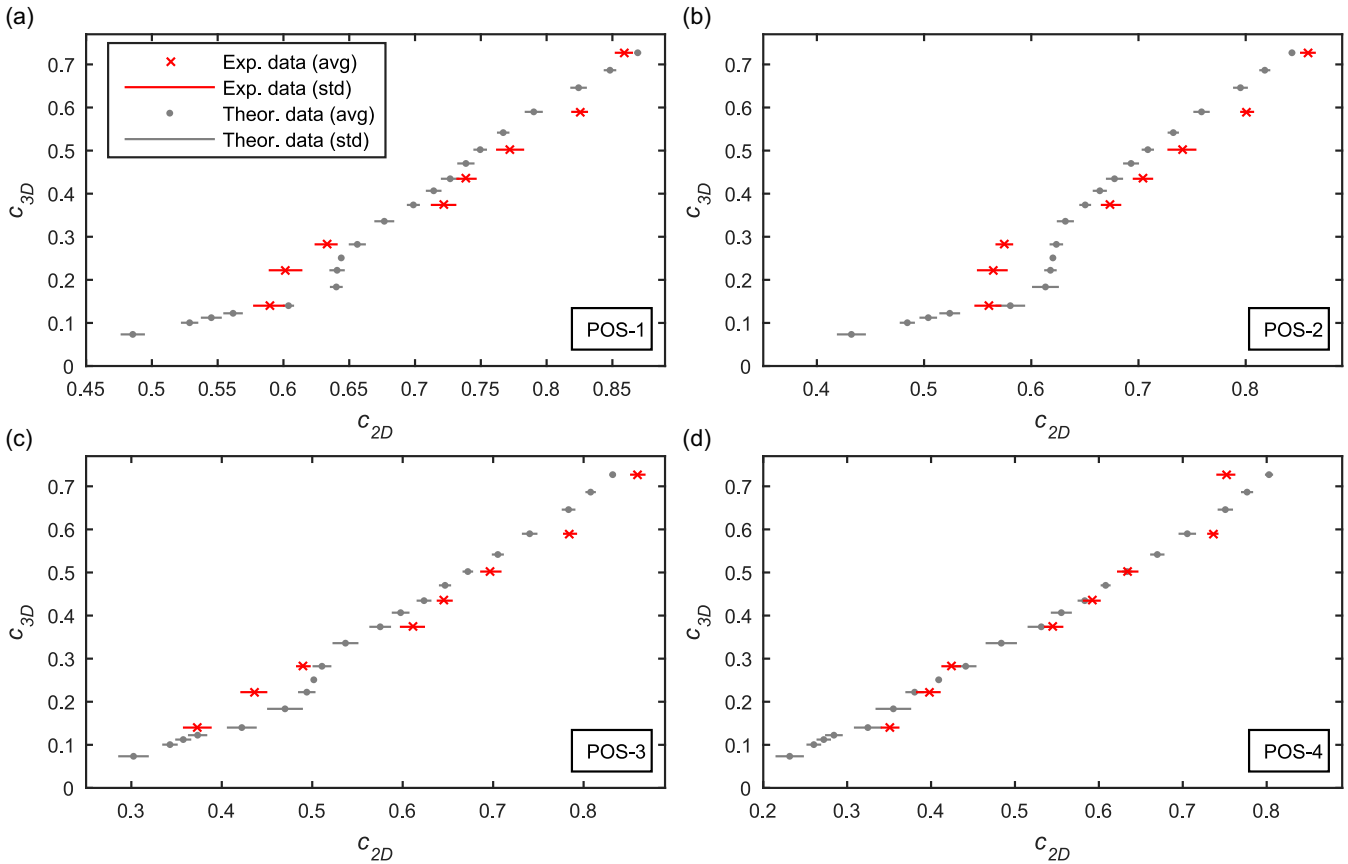
FIG. 7. Comparison between the experimental data (c_{2D}, c_{3D}), obtained by image binarization ($D_N = 1.5d$, $p = 1.0d$), and the corresponding numerical data: (a) POS-1; (b) POS-2; (c) POS-3; (d) POS-4.
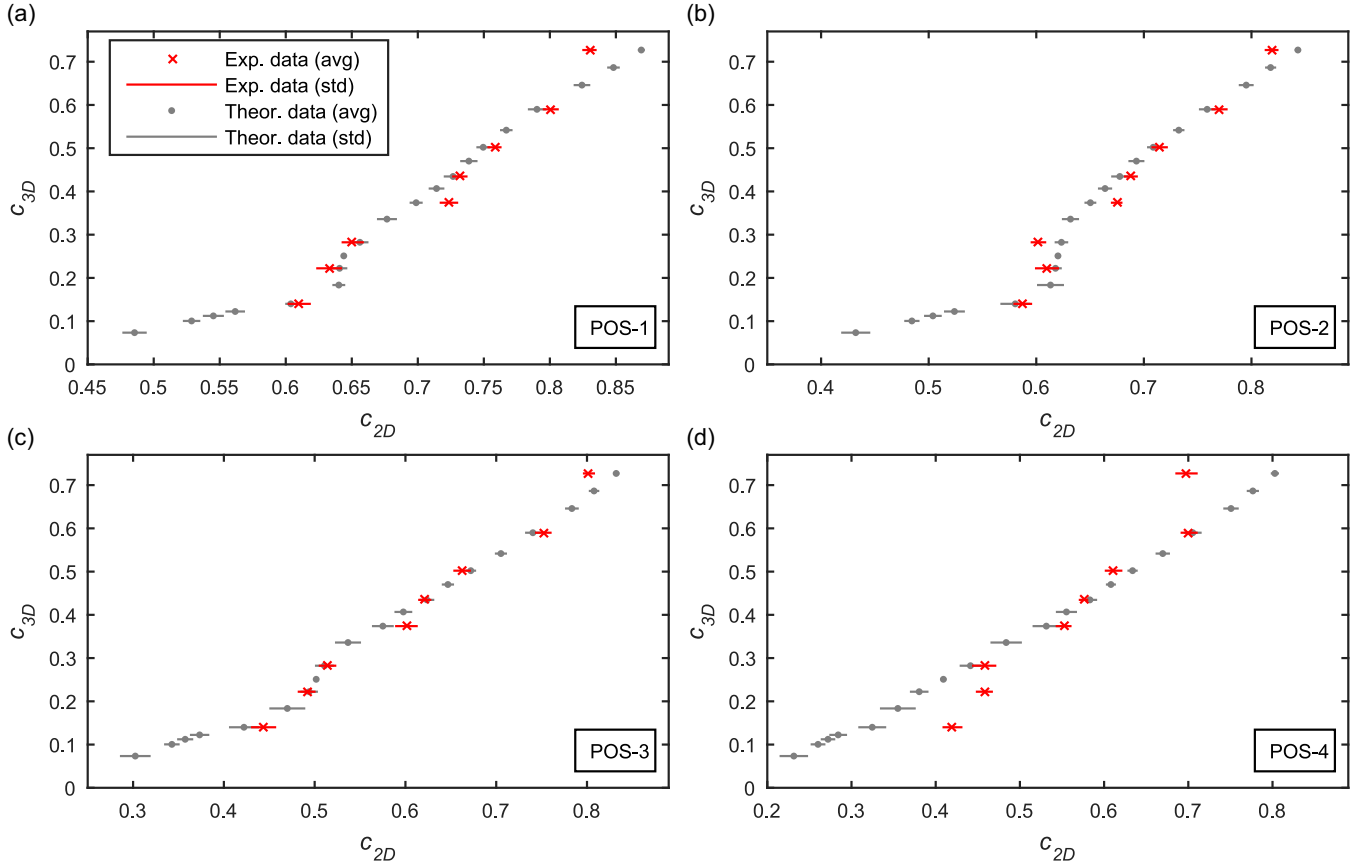
FIG. 8. Comparison between the experimental data (c_{2D}, c_{3D}), obtained by image binarization ($D_N = 1.5d$, $p = 1.5d$), and the corresponding numerical data: (a) POS-1; (b) POS-2; (c) POS-3; (d) POS-4.

investigation exhibit some direct reflectance, which variously influences the optical response of the system at different ζ.

Conversely, by comparing the binarization tests for different values of D_N, we observed very small differences among the binarized images and the resulting RMSE. Nonetheless, from Tables IV–VII it emerges that slightly better results are obtained with $D_N = 1.5d$ and $D_N = 2.0d$. This finding is in agreement with the previous investigations on random granular dispersions [39,40] and confirms that also in the case of FCC lattices the pixel neighborhood, N, has to be sufficiently large to encompass illuminated and nonilluminated surface elements. Focusing on the choice of the MAF, the best overall results are obtained by using $p \approx 1.5d$, with the exception of POS-4, for which $p \approx 1.0d$ is found to be optimal. Conversely, $p < 1.0d$ yields systematically worse results, probably due to the high glare of the spheres (cf. Fig. 5).

In Tables IV–VII it can be also noted that the averaged standard deviation of c_{2D}, $\overline{\sigma_{c_{2D}}}$, slightly increases with D_N, while it decreases with p. Moreover, considering the same binarization settings, it is comforting to notice that the experimental $\overline{\sigma_{c_{2D}}}$ typically increases with ζ, analogous to that already observed numerically [cf. Fig. 3(c)]. Nevertheless, the experimental values of $\overline{\sigma_{c_{2D}}}$ are slightly larger than the theoretical ones, owing to some additional variance introduced by the binarization code. To better illustrate it, comparisons between the experimental and theoretical values of $\overline{\sigma_{c_{2D}}}$ are reported in Fig. 6, where the overall best agreement is obtained with

$D_N = 1.5d$ and $p = 1.5d$. These findings clearly indicate that a relatively large MAF ($\approx 1d - 1.5d$) not only can be safely used in SOM applications but it is also beneficial for improving the accuracy of the binarization task, both in terms of RMSE and of $\overline{\sigma_{c_{2D}}}$. Finally, from Fig. 6 it is interesting to observe that the discrepancy between experimental and theoretical $\overline{\sigma_{c_{2D}}}$ increases with decreasing ζ (with its maximum at $\zeta = 25°$). This extra variance could be explained by the fact that, as it will be discussed in more detail in Sec. IV B, the binarization algorithm occasionally struggles to correctly identify illuminated surface elements of the second and third layers of the lattice, while the relative contribution of these layers to the overall c_{2D} estimation increases with higher penetration depth of the light, corresponding to smaller ζ (cf. Fig. 4).

With reference to the best settings ($D_N = 1.5d$, $p = 1.0d$ and $p = 1.5d$), in Figs. 7 and 8 we report the experimental data (c_{2D}, c_{3D}), in comparison with the theoretical ones, numerically obtained (cf. Sec. III B). Beside the averaged values of c_{2D} (avg) also the standard deviations bands (std) are reported in the same plots. Fig. 7 shows that the setting with $p = 1.0d$ yields optimal results for POS-4. Yet, some underestimations (for S-1, S-2 and S-3) and overestimations (for the other samples with larger c_{3D}) occur for light positions POS-1, POS-2, and POS-3. Conversely, the setting with $p = 1.5d$ (Fig. 8) delivers excellent results for all light positions except POS-4, where c_{2D} overestimations occur for the three most dispersed samples (S-1,
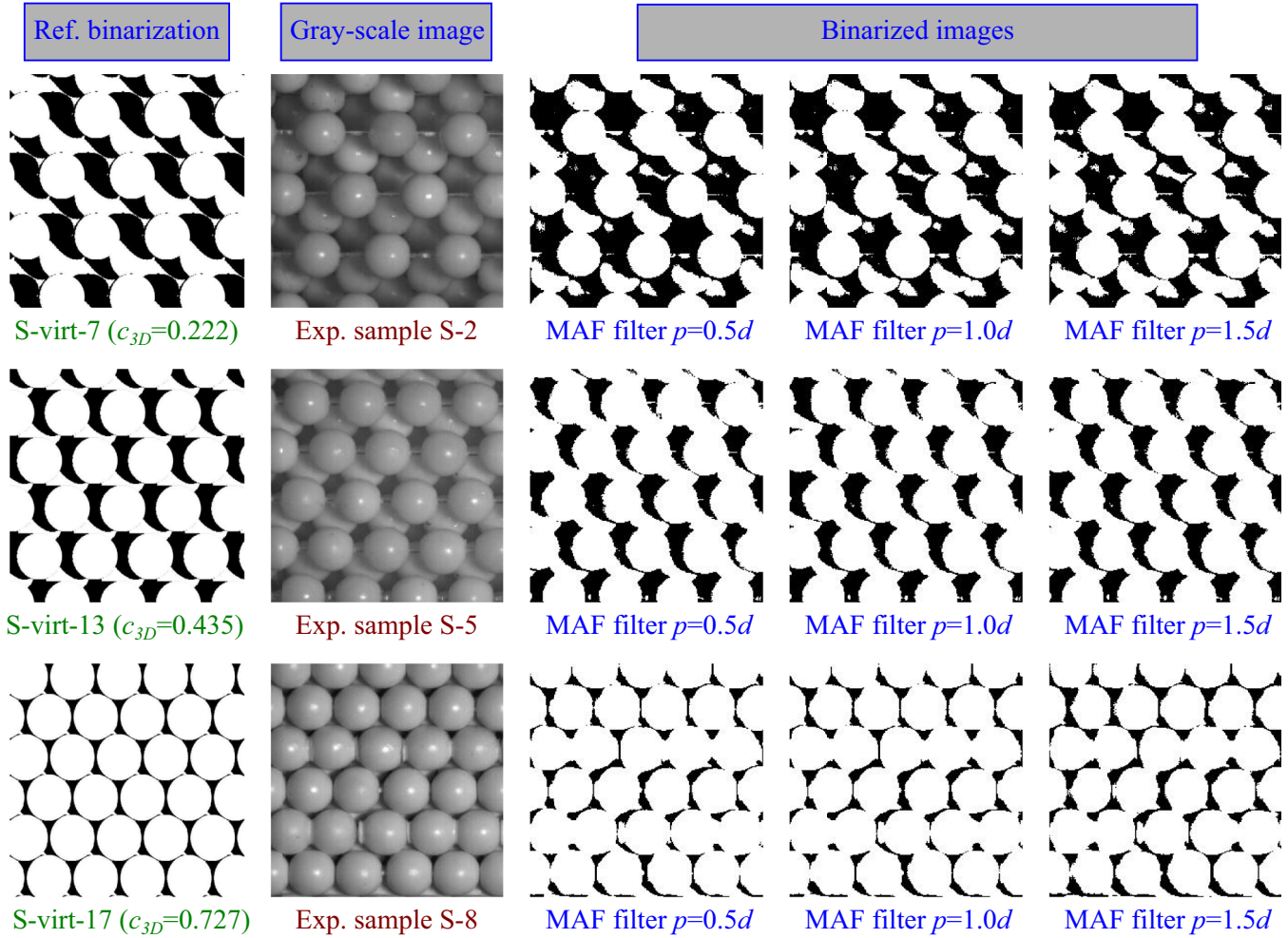
FIG. 9. POS-1: comparisons among binarized images (IW $5d \times 5d$), obtained with $D_N = 1.5d$ and different values of the MAF ($p = 0.5d$, $1.0d$, $1.5d$), and the binary images, obtained numerically.

S-2) and c_{2D} is noticeably underestimated for the densest sample S-8.

As regards the experimental $\sigma_{c_{2D}}(c_{3D})$ reported in Figs. 7 and 8, it is interesting to note that these standard deviations are of the same order of the theoretical ones. Yet, analogous to the $\overline{\sigma_{c_{2D}}}$ values already discussed (cf. Fig. 6), they are occasionally larger than the latter ones, due to some additional variance by the binarization algorithm.

B. Comparisons of the binarized images

Finally, we report the direct comparisons between the experimental binarized images and the corresponding binary images, obtained numerically. For conciseness, we chose to show the two extreme illumination conditions (POS-1 and POS-4) in Figs. 9 and 10, respectively, and three representative samples (S-2, S-5, and S-8). The other samples, as well as the two intermediate illumination conditions, are found to exhibit similar behaviors of those reported in Figs. 9 and 10. For comparison, the binary images, numerically obtained on virtual samples with the same c_{3D} (i.e., S-virt-7, S-virt-13, S-virt-17), are also shown in the same figures. The binarization settings, used here, are $D_N = 1.5d$ and $p = 0.5d$, $1.0d$, $1.5d$.

A generally good agreement was observed for all illumination conditions. Yet, a careful inspection of the images of sample S-2 (Figs. 9 and 10) reveals that the binarization algorithm struggles to correctly identify the illuminated surface elements belonging to the second and third layers of the lattice. Indeed, the pattern of the theoretical binary image is not completely clear in the experimental binarized images, especially in the case of $p = 0.5d$. This problem is mitigated by a larger MAF (cf. Figs. 7 and 8). This issue is mainly due to the fact that, for very dispersed FCC samples ($c_{3D} < 0.3$), there are several surface elements, concurrently visible and illuminated, which are close to each other in the imaging plane but are located at different distances from the wall. This causes strong brightness variations that the binarization code struggles to handle. As regards the other two samples (S-5 and S-8), reported in Figs. 9 and 10 and corresponding to higher c_{3D}, the algorithm is found capable of correctly capturing the c_{2D} patterns. Finally, it is worth mentioning that, for the extreme condition (POS-4) and sample S-8, some overestimation of the shadows in the first layer spheres was typically observed regardless of the size of the MAF [cf. also Figs. 7(d)–8(d)]. This behavior is clearly due to the high glare of the foreground spheres, which, combined with the extreme light position ($\zeta = 38.3°$) renders the use of a

| Ref. binarization | Gray-scale image | Binarized images | | |

S-virt-7 (c_{3D}=0.222) | Exp. sample S-2 | MAF filter p=0.5d | MAF filter p=1.0d | MAF filter p=1.5d

S-virt-13 (c_{3D}=0.435) | Exp. sample S-5 | MAF filter p=0.5d | MAF filter p=1.0d | MAF filter p=1.5d

S-virt-17 (c_{3D}=0.727) | Exp. sample S-8 | MAF filter p=0.5d | MAF filter p=1.0d | MAF filter p=1.5d
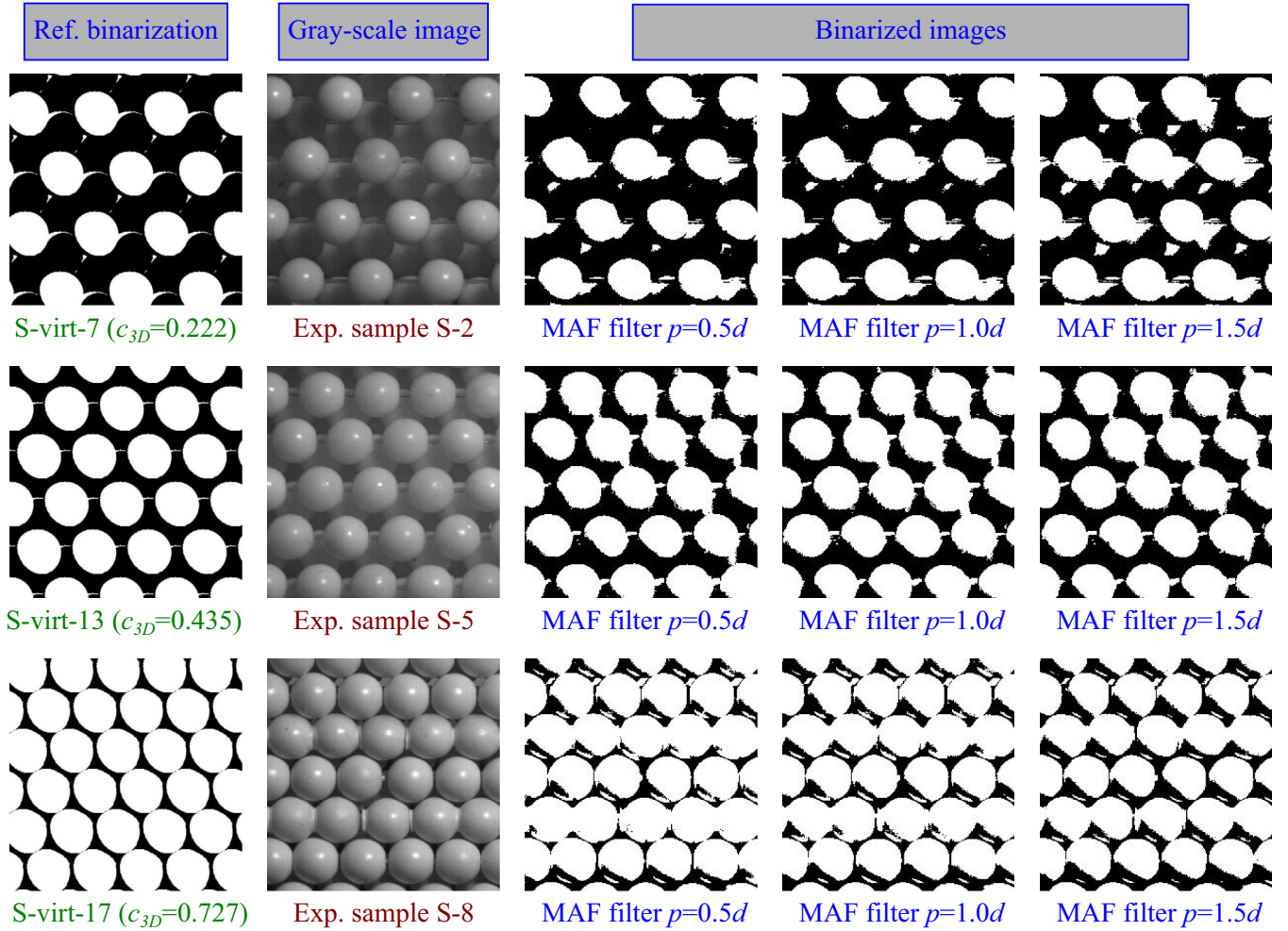
FIG. 10. POS-4: comparisons among binarized images (IW $5d \times 5d$), obtained with $D_N = 1.5d$ and different values of the MAF ($p = 0.5d$, $1.0d$, $1.5d$), and the binary images, obtained numerically.

constant threshold s in Eq. (2) insufficient to provide totally consistent binarization results in the whole investigated c_{3D} interval.

From these comparisons it is confirmed that reasonably good results are obtainable by using the proposed binarization algorithm with $D_N = 1.5d$ and a MAF with $p \approx 1d-1.5d$. Additionally, it can be remarked that a generally better agreement can be easily achieved by choosing relatively small angles of incidence of the light ($\zeta < 35°$), which is especially advisable for the further applications of the SOM method in the presence of direct reflectance of the grains.

V. CONCLUSIONS

This numerical-experimental work focused on the SOM method, proposed by Sarno *et al.* [39] for the measurement of the solid volume fraction in granular media. The method indirectly estimates the near-wall volume fraction, c_{3D}, by means of a correlated quantity, c_{2D}, which is accessible through a suitable image binarization. With the aim of specifically testing the accuracy of the local binarization algorithm, implemented in the SOM, FCC regular lattices of monodisperse spheres were numerically and experimen-

tally investigated. The choice of this setup was motivated by the advantages over random distributions of grains. Indeed, in this case the relationship between c_{2D} and c_{3D} is deterministic. Hence, since all other uncertainties of the SOM method are removed, it was possible to isolate the binarization stage. Moreover, with this setup the binarized images could be directly compared with the numerical ones, so as to better assess the reliability of the binarization algorithm.

Various settings were tested over different light conditions, where, considering the guidelines by Sarno *et al.* [39], an intermediate range for the angle of incidence of the light, $20° < \zeta < 40°$, was investigated. The size of the pixel neighborhood, D_N, was varied between $1.0d$ and $2.0d$, and the MAF, p, proposed for damping out glares, was varied between $0.2d$ and $2.0d$. The comparisons of the experimental data (c_{2D}, c_{3D}) with the numerical ones showed that the best agreement is achieved by using $D_N \approx 1.5-2.0d$. Moreover, the best size of the MAF was $p \approx 1.5d$, except for the extreme lamp position POS-4 ($\zeta = 38.3°$), where $p = 1d$ delivered a better agreement. The comparisons of the experimental standard deviations on c_{2D} with the theoretical values, suggest that some artificial variance, weakly increasing with decreasing ζ,

is introduced by the binarization code. This loss of precision slightly increases with D_N, which led to marginally prefer $D_N \approx 1.5d$ over $D_N \approx 2.0d$. Interestingly, a suitably large MAF is effective to reduce these discrepancies on the c_{2D} standard deviations.

The direct comparisons of the experimental binarized images with the theoretical ones showed that the proposed binarization algorithm generally captures the theoretical patterns and yields sound results for $c_{3D} > 0.3$. It confirms that the method is suitable for the investigation of dense granular systems and granular flows in the dense regime. Nevertheless, some binarization errors arise for the case of highly dispersed FCC samples ($c_{3D} < 0.3$), which indicates that the applicability of the proposed binarization strategy to gas-like granular systems still remains a challenging problem. In particular, the code sometimes fails to correctly identify illuminated surface

elements from different layers of the lattice, due to noticeable brightness variations. This problem is partially mitigated by an opportune choice of the MAF size.

Overall, this work proves the general suitability of the proposed binarization algorithm with a RMSE on c_{2D} always smaller than 0.03. On the other hand, it highlights the importance of opportunely choosing the binarization parameters. The development of more sophisticated automatic-vision binarization algorithms may further increase the accuracy, achievable by the SOM method.

[1] J. T. Jenkins and S. B. Savage, A theory for the rapid flow of identical, smooth, nearly elastic, spherical particles, J. Fluid Mech. **130**, 187 (1983).

[2] P. Jop, Rheological properties of dense granular flows, C. R. Phys. **16**, 62 (2015).

[3] S. Lanzoni, C. Gregoretti, and L. M. Stancanelli, Coarse-grained debris flow dynamics on erodible beds, J. Geophys. Res. Earth Surf. **122**, 592 (2017).

[4] R. Delannay, A. Valance, A. Mangeney, O. Roche, and P. Richard, Granular and particle-laden flows: From laboratory experiments to field observations, J. Phys. D **50**, 053001 (2017).

[5] L. Sarno, L. Carleo, M. N. Papa, and P. Villani, Experimental investigation on the effects of the fixed boundaries in channelized dry granular flows, Rock Mech. Rock Eng. **51**, 203 (2018).

[6] A. Armanini, H. Capart, L. Fraccarollo, and M. Larcher, Rheological stratification in experimental free-surface flows of granular-liquid mixtures, J. Fluid Mech. **532**, 269 (2005).

[7] A. Armanini, L. Fraccarollo, and M. Larcher, Liquid–granular channel flow dynamics, Powder Technol. **182**, 218 (2008).

[8] L. Sarno, A. Carravetta, R. Martino, and Y. C. Tai, A two-layer depth-averaged approach to describe the regime stratification in collapses of dry granular columns, Phys. Fluids **26**, 103303 (2014).

[9] D. Gollin, W. Brevis, E. T. Bowman, and P. Shepley, Performance of PIV and PTV for granular flow measurements, Granul. Matter **19**, 42 (2017).

[10] L. Sarno, A. Carravetta, R. Martino, M. N. Papa, and Y. C. Tai, Some considerations on numerical schemes for treating hyperbolicity issues in two-layer models, Adv. Water Resour. **100**, 183 (2017).

[11] M. N. Papa, L. Sarno, F. Vitiello, and V. Medina, Application of the 2D depth-averaged model, FLATModel, to pumiceous debris flows in the Amalfi Coast, Water **10**, 1159 (2018).

[12] S. Meninno, A. Armanini, and M. Larcher, Gravity-driven, dry granular flows over a loose bed in stationary and homogeneous conditions, Phys. Rev. Fluids **3**, 024301 (2018).

[13] Y. C. Tai, J. Heß, and Y. Wang, Modeling two-phase debris flows with grain-fluid separation over rugged topography: Application to the 2009 Hsiaolin Event, Taiwan, J. Geophys. Res. Earth Surf. **124**, 305 (2019).

[14] P. A. Cundall and O. D. Strack, A discrete numerical model for granular assemblies, Geotechnique **29**, 47 (1979).

[15] J. W. Landry, G. S. Grest, L. E. Silbert, and S. J. Plimpton, Confined granular packings: Structure, stress, and forces, Phys. Rev. E **67**, 041303 (2003).

[16] L. Lacaze, J. C. Phillips, and R. R. Kerswell, Planar collapse of a granular column: Experiments and discrete element simulations, Phys. Fluids **20**, 063302 (2008).

[17] C. Y. Kuo, L. T. Sheng, S. Y. Chiu, Y. Z. Yang, Y. C. Tai, and S. S. Hsiau, Measurement and discrete element simulation of a fixed-obstacle disturbed rapid granular chute flow, Phys. Fluids **27**, 013305 (2015).

[18] Y. C. Chung, C. W. Wu, C. Y. Kuo, and S. S. Hsiau, A rapid granular chute avalanche impinging on a small fixed obstacle: DEM modeling, experimental validation and exploration of granular stress, Appl. Math. Model. **74**, 540 (2019).

[19] H. Capart, D. L. Young, and Y. Zech, Voronoï imaging methods for the measurement of granular flows, Exp. Fluids **32**, 121 (2002).

[20] B. Spinewine, H. Capart, M. Larcher, and Y. Zech, Three-dimensional Voronoï imaging methods for the measurement of near-wall particulate flows, Exp. Fluids **34**, 227 (2003).

[21] M. M. Cui and R. J. Adrian, Refractive index matching and marking methods for highly concentrated solid-liquid flows, Exp. Fluids **22**, 261 (1997).

[22] M. Moroni, N. Kleinfelter, and J. H. Cushman, Analysis of dispersion in porous media via matched-index particle tracking velocimetry experiments, Adv. Water Resour. **30**, 1 (2007).

[23] W. J. Ni and H. Capart, Cross-sectional imaging of refractive-index-matched liquid-granular flows, Exp. Fluids **56**, 163 (2015).

[24] J. E. Maneval, K. M. Hill, B. E. Smith, A. Caprihan, and E. Fukushima, Effects of end wall friction in rotating cylinder granular flow experiments, Granul. Matter **7**, 199 (2005).

[25] L. Sarno, L. Carleo, M. N. Papa, and P. Villani, Optical measurements of velocity and of solid volume fraction in fast dry granular flows in a rectangular chute, in *Proceedings of the 7th International Conference on Debris-Flow Hazards Mitigation*, edited by J. W. Kean, J. A. Coe, P. M. Santi, and B. K. Guillen (Association of Environmental and Engineering

Geologists, Colorado School of Mines, Golden, 2019), Vol. 28, p. 429.

[26] N. Brodu, R. Delannay, A. Valance, and P. Richard, New patterns in high-speed granular flows, J. Fluid Mech. **769**, 218 (2015).

[27] N. Jesuthasan, B. R. Baliga, and S. B. Savage, Use of particle tracking velocimetry for measurements of granular flows: Review and application - particle tracking velocimetry for granular flow measurements, Kona **24**, 15 (2006).

[28] W. Eckart, J. M. N. T. Gray, and K. Hutter, Particle image velocimetry (PIV) for granular avalanches on inclined planes, in *Dynamic Response of Granular and Porous Materials Under Large Catastrophic Deformations*, edited by K. Hutter and N. Kirchner, Lecture Notes in Applied and Computational Mechanics Vol. 11 (Springer, Berlin, 2003).

[29] S. P. Pudasaini, S. S. Hsiau, Y. Wang, and K. Hutter, Velocity measurements in dry granular avalanches using particle image velocimetry technique and comparison with theoretical predictions, Phys. Fluids **17**, 093301 (2005).

[30] A. Armanini, M. Larcher, E. Nucci, and M. Dumbser, Submerged granular channel flows driven by gravity, Adv. Water Res. **63**, 1 (2014).

[31] N. Sanvitale and E. T. Bowman, Using PIV to measure granular temperature in saturated unsteady polydisperse granular flows, Granul. Matter **18**, 57 (2016).

[32] L. Sarno, A. Carravetta, Y.-C. Tai, R. Martino, M. N. Papa, and C.-Y. Kuo, Measuring the velocity fields of granular flows– Employment of a multi-pass two-dimensional particle image velocimetry (2D-PIV) approach, Adv. Powder Tech. **29**, 3107 (2018).

[33] L. Sarno, Y. C. Tai, A. Carravetta, R. Martino, M. N. Papa, and C. Y. Kuo, Challenges and improvements in applying a particle image velocimetry (PIV) approach to granular flows, J. Phys. Conf. Ser. **1249**, 012011 (2019).

[34] T. G. Drake, Structural features in granular flows, J. Geophys. Res. B **95**, 8681 (1990).

[35] H. Ahn, C. E. Brennen, and R. H. Saversky, Measurements of velocity, velocity fluctuation, density, and stresses in chute flows of granular materials, J. Appl. Mech. **58**, 792 (1991).

[36] M. Barbolini, A. Biancardi, L. Natale, and M. Pagliardi, A low cost system for the estimation of concentration and velocity profiles in rapid dry granular flows, Cold Reg. Sci. Technol. **43**, 1 (2005).

[37] B. Spinewine, H. Capart, L. Fraccarollo, and M. Larcher, Laser stripe measurements of near-wall solid fraction in channel flows of liquid-granular mixtures, Exp. Fluids **50**, 1507 (2011).

[38] L. T. Sheng, C. Y. Kuo, Y. C. Tai, and S. S. Hsiau, Indirect measurements of streamwise solid fraction variations of granular flows accelerating down a smooth rectangular chute, Exp. Fluids **51**, 1329 (2011).

[39] L. Sarno, M. N. Papa, P. Villani, and Y.-C. Tai, An optical method for measuring the near-wall volume fraction in granular dispersions, Granul. Matter **18**, 80 (2016).

[40] L. Sarno, M. N. Papa, Y. C. Tai, L. Carleo, and P. Villani, A non-invasive stochastic-optical method (SOM) for estimating the volume fraction in granular flows: Application on interrogation windows with different aspect ratios, J. Phys. Conf. Ser. **1249**, 012013 (2019).

[41] L. Carleo, L. Sarno, M. N. Papa, Y.-C. Tai, and P. Villani, Volume fraction and velocity fields of nearly uniform granular flows in a narrow channel geometry with smooth bed, Adv. Powder Tech. **30**, 2379 (2019).

[42] H. Kahmen and W. Faig, *Surveying* (Walter de Gruyter Inc., Berlin, 1988).

[43] J. Kepler, *Strena Seu De Nive Sexangula* (Frankfurt, Germany, 1611).

[44] T. Hales *et al.*, A formal proof of the Kepler conjecture, Forum Math., Pi **5**, E2 (2017).

[45] R. A. Bagnold, Experiments on a gravity-free dispersion of large solid spheres in a Newtonian fluid under shear, Proc. Roy. Soc. London A **225**, 49 (1954).